Femto-Laser Processed Metasurface With Fano Response: Applications to a High Performance Refractometric Sensor

Mahmoud H. Elshorbagy[1,2*], Alejandro San-Blas[3,4] , Luis Miguel Sanchez-Brea[5], Santiago M. Olaizola[3,4], Jesús del Hoyo[5], Angela Soria-Garcia[5], Joaquin Andres-Porras[5], Verónica Pastor-Villarrubia[2], and Javier Alda[2]

[1]*Physics Department, Faculty of Science, Minia University, El Minia 61519, Egypt*

[2]*Applied Optics Complutense Group, Faculty of Optics and Optometry, Universidad Complutense de Madrid, Madrid 28037, Spain*

[3]*Ceit-Basque Research and Technology Alliance, Donostia-San Sebastian 20018, Spain*

[4]*Electrical and Electronic Engineering Department, Universidad de Navarra, Donostia-San Sebastian 20018, Spain*

[5]*Applied Optics Complutense Group, Optics Department, Faculty of Physics, Universidad Complutense de Madrid, Madrid 28040, Spain*

[*]Corresponding author: Mahmoud H. Elshorbagy E-mail: m.s.elshorbagy@mu.edu.eg

Abstract: The practical development of compact modern nanophotonic devices relies on the availability of fast and low-cost fabrication techniques applicable to a wide variety of materials and designs. We have engraved a split grating geometry on stainless steel using femtosecond laser processing. This structure serves as a template to fabricate efficient plasmonic sensors, where a thick gold layer is grown conformally on it. The scanning electron microscope (SEM) images confirm the generation of the split laser-induced periodic spatial structures. The optical reflectance of our sensors shows two dips corresponding to the excitation of surface plasmon resonances (SPRs) at two different wavelengths. Furthermore, the asymmetric shape of these spectral responses reveals a strong and narrow Fano resonance. Our computational electromagnetism models accurately reproduce the reflectivity of the fabricated structure. The spectral responses of both the simulated and fabricated structures are fitted to the Fano model that coherently combines the narrow SPRs with the broad continuum background caused by diffraction. The parameters extracted from the fitting, such as the resonance wavelengths and line widths, are used to evaluate the performance of our device as a refractometric sensor for liquids. The maximum sensitivity and figure of merit are 880 nm/RIU and 80 RIU^{-1}, respectively. Besides the compact design of our sensing device, its performance exceeds the theoretical maximum sensitivity of a classical Kretschmann setup.

Keywords: Plasmonics; refractometric sensing; Fano resonances; laser-induced periodic surface structures

Citation: Mahmoud H. ELSHORBAGY, Alejandro SAN-BLAS, Luis Miguel SANCHEZ-BREA, Santiago M. OLAIZOLA, Jesús del HOYO, Angela SORIA-GARCIA, *et al*., "Femto-Laser Processed Metasurface With Fano Response: Applications to a High Performance Refractometric Sensor," *Photonic Sensors*, 2025, 15(2), 250228.

Received: 18 September 2023 / Revised: 1 March 2024

DOI: 10.1007/s13320-024-0736-y
Article type: Regular

1. Introduction

Metasurfaces and metamaterials are at the core of modern and efficient nanophotonic devices [1–3]. Their capabilities to manage light are based on the light-matter interaction at the subwavelength scale, which generates light trapping, surface plasmon resonances (SPRs), and customized spectral responses [4–8]. The SPR mechanism allows the measurement and monitoring of the index of refraction of materials in chemistry [9, 10], biology [11, 12], and environmental sciences [13], as a real-time and label-free technique. The practical realization of nanostructures requires a precise combination of geometry, materials, and fabrication tools. On the one hand, the choice of geometry and materials should respond to prescribed specifications in the optical response of the device. On the other hand, the manufacturing method determines the cost, feasibility, and practical throughput of the production, and has an impact on the overall performance of the finished device. As a low-cost manufacturing micro- and nano-structuring technique, femtosecond laser ablation modifies the topography of the surface of substrates allowing advanced applications at a lower cost than other high-end nano-fabrication methods based on e-beam lithography, or focused ion beam techniques [14–17]. Femtosecond laser ablation and nano-structuring is a fast and affordable nano-fabrication technique, at the cost of some inhomogeneities and variability [18–20]. The parameters of the laser pulse (the duration, repetition rate, number of pulses, fluence, polarization state, etc.) can be tuned to improve the quality and reproducibility of the finished nanostructure generated on a given material [21–25]. In the end, both ablation and thermal effects modify the surface structure at the micro and nano scales [26–29].

In this contribution, we are interested in the formation of laser-induced periodic spatial structures (LIPSSs) which are easily and more efficiently generated in metallic substrates for a precise combination of the beam parameters [30–32]. The LIPSS takes the form of a grating with a period related to the laser wavelength with an orientation depending on the polarization state of the ablation beam. The LIPSS profile is commonly modeled as having simple triangular, rectangular, or cylindrical shapes [33], or more complex two-dimensional (2D) geometries [34, 35]. Besides modifying the surface finishing [36, 37], the LIPSS works as polarizing optical elements [38], antireflection coatings [39, 40], and plasmonic sensors [41]. These complex nanostructures can also be produced using high-resolution techniques, such as lithography and self-assembly methods [42] at a high cost with low fabrication throughput. In comparison, femtosecond laser processing has the advantage of being low-cost, fast, and applicable to large-scale production.

This paper is focused on the use of the LIPSS, generated by femtosecond laser ablation, as a refractometric sensor of liquids. Our design improves the performance of this type of sensing device by optimizing the values of the sensitivity, figure of merit (FOM), linearity, limit of detection, and detection range of the sensor [43–45]. Our sensor uses low-cost stainless steel substrates to fabricate customized LIPSSs. The generated profile serves as a template to conformally grow a thin gold layer to enhance the spectral response of the device due to SPR generation. The broad-band diffractive background of the LIPSS grating interferes coherently with the narrow spectral plasmonic resonance to produce a Fano-like spectral response. The resulting asymmetric lineshape is highly sensitive to any change in the index of refraction at the interface of the plasmonic structure.

After this introduction, Section 2 describes the fabrication methods and materials, and the geometric characterization of the topography. Section 3 is devoted to the analysis of the optical response of the fabricated device compared with the results from computational electromagnetism

simulations. This study also includes a fitting of the observed response with a Fano-type resonance. The performance of the device as a refractometric plasmonic sensor for liquids is reported in Section 4, showing how the model and the experimental results fit well and allow us to predict better performance of the device in the infrared region (IR). Finally, Section 5 summarizes the main conclusions of this contribution.

2. Fabrication and topographic parameterization

The femtosecond laser ablation is made on a stainless steel substrate (AISI 304) having a roughness characterized by R_a≈27.63 nm. This substrate has been selected because it is cheap and reflective, because the generated LIPSS is more regular in stainless steel than in other metals due to the presence of short-range surface plasmon polaritons [20]. Before ablation, the sample is sonicated for 3 minutes in an acetone bath to remove organic contaminants, dirt, and debris. Then, the sample is rinsed in distilled water and dried by blowing pressurized air on it. We have used a titanium-sapphire (Ti:sapphire) laser with a nominal pulse duration of 120 fs at a central wavelength (λ=800 nm) having a repetition frequency of 1 kHz. The energy of the pulse is controlled with a half-wave plate and a polarizing beam splitter. The laser beam is focused on the sample through a cylindrical lens with f=100 mm, and its spatial irradiance distribution is monitored by a dedicated charge coupled device (CCD) camera. Due to the cylindrical lens, the irradiance distribution is highly elliptical with a radius at the $1/e^2$ level of w_x=54.5 μm and w_y=6 mm, being x the scanning direction. This elliptical spot allows the generation of the LIPSS on a large area in a single pass at higher speeds, when compared with the LIPSS fabricated using circular irradiance distributions. In our case, we have selected a pulse energy of E=0.55 mJ, with a number of pulses per spot of N=174 pulses. These parameters produce an average fluence per pulse of 53.5 mJ/cm^2 on a sample that moves along the x-axis with the speed v=0.625 mm/s. The polarization of the beam is linear and oriented along the scanning direction. Figure 1 shows the fabricated setup and how the substrate is scanned under the laser beam to generate the LIPSS.

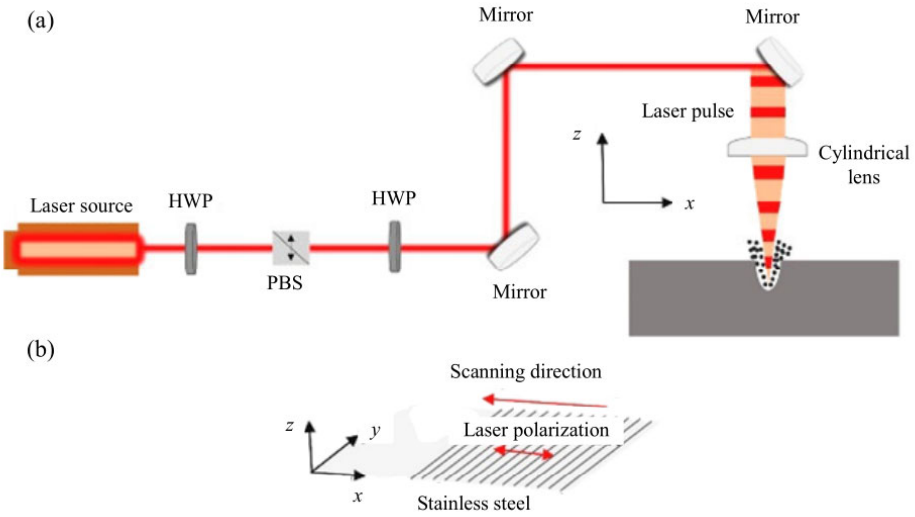

Fig. 1 Fabrication setup: (a) schematic diagram of the fabrication setup with all the elements involved in the process: lenses, mirror, and polarization control components: half-wave plate (HWP) and polarizing beam splitter (PBS) and (b) illustration of the scanning direction with respect to the moving stage.

The LIPSS generated using the technique presented here is quite regular and presents a shallow groove in the middle, showing signs of splitting. This structure is caused by the formation of the type-2s LIPSS, and it is known as split-LSF-LIPSS [46]. The generation of this topography can be explained by an inter-pulse feedback mechanism and happens for a high number of pulses within a narrow fluence range only, as it happens in our experimental setup [47]. Our device uses stainless steel due to the good homogeneity of the LIPSS fabricated on this type of substrate. On the top of the nano-structured stainless steel surface, we sputter a 300 nm thick gold layer that maintains the LIPSS topography under it. This addition improves the performance of the device. First, the low reflectivity of stainless steel is replaced by the larger reflectivity of gold, and then the gold coating generates a good plasmonic response [48] which is able to detect changes in the index of refraction of the analyte in contact with it. Moreover, gold shows very good chemical and biological compatibility to serve as an appropriate material to interact with biological samples [49].

2.1 Analysis of the topography

Despite the large-scale fabrication capabilities of the femtosecond laser technique, the generated LIPSS may have some irregularities or imperfections, which can be mitigated to smooth the resulting topography [18–21]. The reliability of the gold coating has required some previous characterization of the deposition process. We use a flat stainless steel substrate to sputter gold and measure its thickness using a surface profilometer. Through this calibration, the thickness of the gold layer is given as a function of the deposition rate and time. As a final check-up, we process the coated LIPSS with the focused ion beam to reveal a cross section that is characterized through the scanning electron microscope (SEM). Gold layers with different thicknesses are deposited on the top of the stainless steel LIPSS. In Fig. 2(a) we show four cases of gold thicknesses (t_{Au}=100 nm, 260 nm, 305 nm, and 420 nm). These samples show the LIPSS structures on stainless steel with an average period of 695 nm and an average height of 100 nm. From the point of view of cost optimization, the thickness of the gold layer could be reduced significantly while maintaining a negligible transmission of light towards the underlying stainless steel nanostructure. However, the optical response also depends on the thickness of the gold layer [see the experimental spectral reflectance plotted in Fig. 2(b)]. For coatings up to 260 nm, we find a sharper Fano resonance when the thickness is increased. At the same time, Fig. 2(a) shows how the deposition is quite conformal for thicknesses of 100 nm and 260 nm. This conformality smooth as

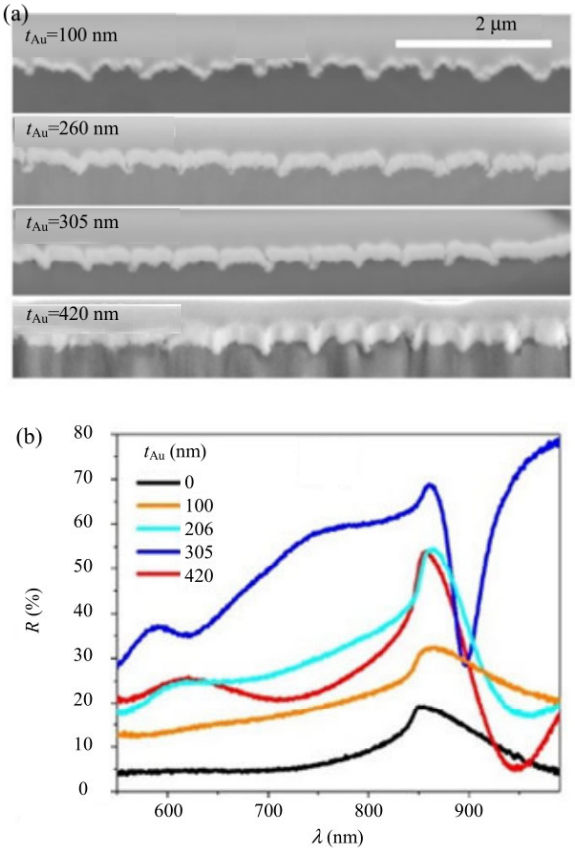

Fig. 2 Cross section and spectral characterization of gold-coated LIPSS: (a) cross section of the fabricated samples showing the underlying LIPSS and the gold layer for several values of the thicknesses of the coating and (b) experimental spectral reflectance of samples with different gold thicknesses.

the gold layer is thicker. The result is that the grooves between adjacent LIPSSs narrow, generating nano-grooves with a higher aspect ratio. This trend is broken above 300 nm of gold coating. We can see in Fig. 2(a) how the conformality does not apply for a 400 nm thick coating: the nano-grooves disappear, and the optical response broadens.

Figure 3 shows the topography of the fabricated LIPSS. The SEM images in Figs. 3(a) and 3(c) reveal the splitting feature of a highly regular LIPSS grating. In Fig. 3(b), we have depicted how a geometrical model resembles a three-dimensional (3D) smooth version of the actual profile. This representation is used in our 2D computational electromagnetism calculation to obtain the spectra response of the structure. The 2D unit cell is shown in Fig. 3(d).

The profile has been modeled as a combination of two super-Gaussian functions [38]. A wide super-Gaussian function reproduces the main LIPSS profile and a second one is used to model the dip caused by the splitting of the grating. The analytical model is given as

$$h(x) = h_1 \exp\left[-\left(\frac{x^2}{\sigma_1^2}\right)^{\beta_2}\right] - h_2 \exp\left[-\left(\frac{x^2}{\sigma_2^2}\right)^{\beta_2}\right]. \quad (1)$$

The two Gaussian widths, σ_1 and σ_2, adjust the width of the profile and the middle dip, respectively. The amplitudes, h_1 and h_2, describe the depth of the larger profile and the dip, respectively. The power of the two super-Gaussian functions, β_1 and β_2, reproduce the sharpness of the profile. The graphical layout of the fitted profile is presented in Fig. 3(d).

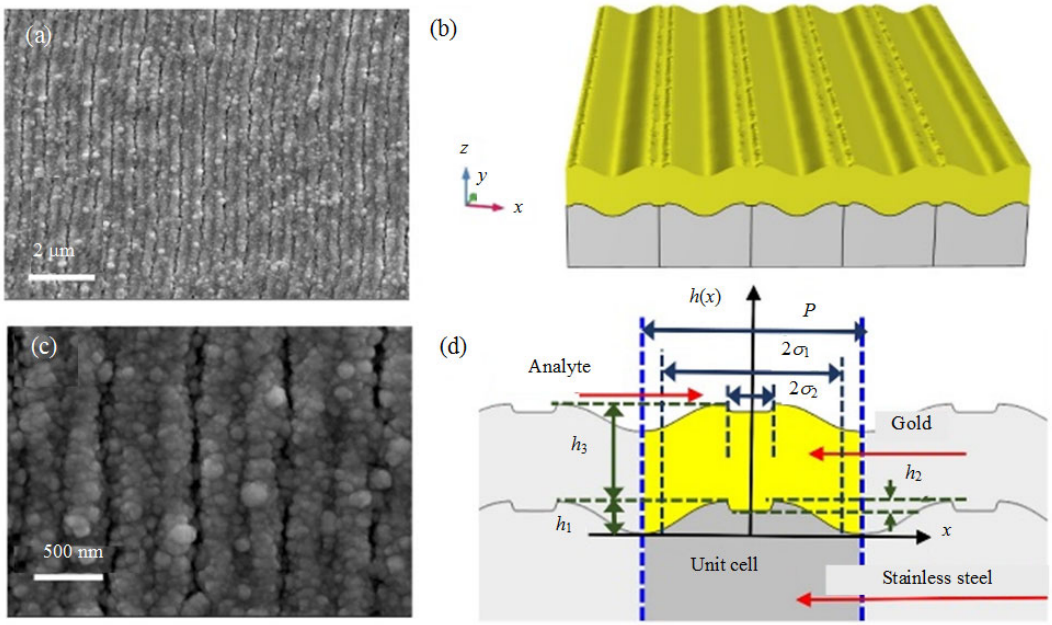

Fig. 3 Topographic characterization: (a) and (c) scanning electron microscope images for the fabricated sample with two magnifications to show the regularity at the large scale and clear view of the split LIPSS, (b) 3D representation of the simulated structure that replicates the fabricated morphology, and (d) geometrical parameters of the unit cell used for the optical model.

The values for the parameters in (1) are h_1=100 nm, h_2=20 nm, σ_1=234.5 nm, σ_2=52 nm, β_1=10, and β_2=10, for a grating period of P=695 nm (see Table 1). Assuming a conformal deposition of the gold layer, the exposed topography is $h(x)+h_3$, where h_3=305 nm is the thickness of the Au coating. From the top to the bottom, the materials are arranged as follows: the analyte medium next to the illumination source and detector domains, a gold layer, and a stainless steel substrate. The gold coating is thick enough to prevent any transmission. Besides, any residual transmission through gold is

absorbed by the substrate.

The structure is modeled using the computational electromagnetism module of COMSOL Multiphysics. In our simulations, we have a tunable monochromatic light source with transversal magnetic (TM) polarization illuminating the unit cell with a variable angle of incidence. The listening port is located on the top to collect the reflected light under mirror reflection conditions. For the TM mode, the ports are defined using a magnetic field amplitude of (0,0,1) A/m, and the angle of incidence of the incoming waves. Then, by dividing the whole geometry into tiny domains through meshing, the finite element method solves Maxwell's equations to evaluate the fields at each point of the structure. Once we have these fields, we calculate the optical parameters of interest, such as transmission, reflection, or absorption. The periodicity is modeled using only one unit cell and applying the Floquet boundary conditions to mimic the actual sample with the period P [see Fig. 3(d)]. This approach takes advantage of the field continuity across the lateral walls of the unit cell. Due to the symmetry of the structure, we can evaluate the performance of the infinite periodic structure by solving the problem for one unit cell only. The model is terminated on the top and bottom by two perfect-matched layers (PML) to absorb higher diffraction orders that could interact with the low-order diffraction orders of interest. The orientation of these PMLs is adjusted for each wavelength and angle of incidence. The COMSOL package can solve Maxwell's equations for the fields when every element has a maximum size at least five times smaller than the wavelength. For more accuracy, we use a maximum element size of $\lambda/10$ in the whole model and increase the meshing density in the locations of thin layers and tiny regions of the gratings. The final geometrical parameters are listed in Table 1. The optical constant of the stainless steel is experimentally measured, and the parameters for gold are obtained in [50].

Table 1 Geometrical and material arrangement of the device (top to bottom).

Layer	Thickness and geometry parameters
Analyte (initially air n_a=1.0)	Infinite
Gold (thin film)	h_3=305 nm
Stainless steel (substrate)	Infinite
LIPSS-main	σ_1=234.5 nm and h_1=100 nm, β_1=2 and P=695 nm
LIPSS-split	σ_2=52 nm, h_2=20 nm, and β_2=10

3. Spectral response

The spectral response of the fabricated device is analyzed for its use in optical sensing. We have experimentally measured the spectral reflectance in air for several angles of incidence, ϕ. The device is illuminated by a super-continuum laser (NKT Photonics, SuperK Compact) emitting in a wide spectral range, $\lambda \in$ [450 nm, 2 400 nm], and coupled to a fiber. The linear polarization of the laser is adjusted to excite the TM mode. The mirror reflection is collected by a fiber coupled to a visible and near-infrared spectrometer (Oriel, MS257). Both illumination and collection fibers are mounted on a θ–2θ mechanical arm. This setup eases the correct collection of the reflected signal. The experimental results in the visible are shown as a red dashed-dotted line in Fig. 4 for twelve angles of incidence from ϕ=25º up to ϕ=80º. Using the geometric and material arrangement presented in subsection 2.1, we have simulated the structure to reproduce the experimental results plotted as a blue dashed-dotted line in Fig. 4. The experimental results in the near infrared are presented in the first row of Fig. 5. For both the visible and infrared spectra, the location of the spectral minimum obtained from simulation agrees well with the experimental results. However, the shape of the simulated reflectance is sharper than the experimental result. These discrepancies are mostly caused by the inherent irregularities of the fabricated device against the perfect geometry used in the simulation. Both in the simulation and experiment, there is a first peak within the visible (see Fig. 4)

and a second one in the near infrared (see Fig. 5). These peaks become narrower and red-shifted when increasing the angle of incidence [51], as it happens with the previously reported SPR sensor, where the performance gets better for a larger angle of incidence or longer wavelengths [52, 53]. Due to the spectral range limitations, the resonance in the near infrared is only measured up to ϕ=20º. Beyond this angle of incidence, the resonance lies above the maximum measurable wavelength of our spectrometer. In our analysis, after validating the simulated results against the experiment, we can extend the spectral range of interest beyond our experimental limitations through simulation. The results for three angles of incidence are given in the second row of Fig. 4, showing the same trend as in the visible: the resonance red shifts and its spectral width decreases as the angle of incidence increases.

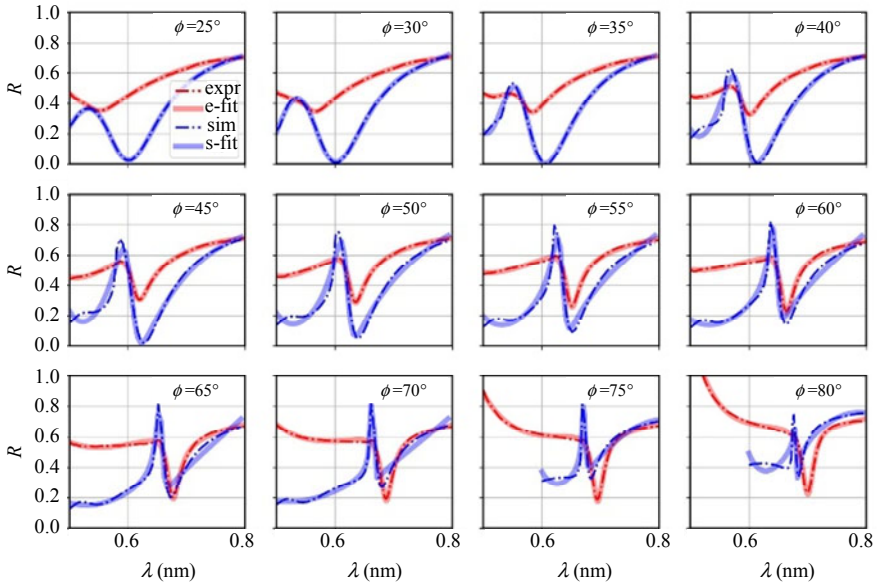

Fig. 4 Spectral reflectance for the device under analysis in the visible range. The experimental results (expr) are plotted in red dashed-dot line with its fitting (e-fit) as a solid semitransparent red line. The simulated response (sim) is given as a blue dashed-dot line with the fitting (s-fit) as a solid semitransparent blue line (see legend at the upper-left corner subplot). These plots are for 12 angles of incidence varying from ϕ =25º up to ϕ =80º and for the same spectral range between 500 nm and 800 nm.

The peaks found in the reflectance are not symmetric and can be explained as the Fano resonances where the narrow SPR lineshape combines coherently with the broader diffractive response of the grating. To check this previous assumption, we have fitted the experimental reflectance to a Fano model applicable to our structure. This model can be written as

$$r_d = r_{\mathrm{bk}} + \sum_{j=1}^{M} f_j \frac{\Omega_j}{(\omega - \omega_{0,j})\mathrm{i} + \Omega_j}, \qquad (2)$$

where r_d is the reflection coefficient, f_j is the complex Fano coupling coefficient, Ω_j is the width of the Lorentzian term, i is imaginary unit, and ω is the angular frequency of the incident light. The sum over j in (2) describes M Lorentzian-shaped SPRs that could appear in the spectral range of interest, where M typically varies between 1 and 3, and j=1 is the most relevant SPR. In the case treated in this paper, we have only considered one resonance, meaning M=1.

The first term, r_{bk}, represents the wide spectral diffractive response due to the grating. This term is given as a Fourier series expansion around the central frequency of the strongest SPR, $\omega_{0,1}$, that includes up to the cubic order terms in ω. The result of this fitting can be seen as thick semitransparent lines in Figs. 4 and 5 for the visible and the near infrared, respectively. These figures also show how the resonance narrows when the angle of incidence

increases. We have fitted the model in (2) to the experimental and simulated spectra for the 12 angles of incidence considered in our analysis in the visible range (see Fig. 4) and for the 6 angles of incidence in the near infrared (see Fig. 5). We can check that for a small angle of incidence, the spectral reflectivity shows a wide and flat resonance, where the slow varying term, r_{bk}, is dominant. However, for a large angle of incidence, the peak becomes steeper and narrower, indicating the growing importance of the Lorentzian shape of the involved SPR. From the fitting, we can extract the values of ω_0 and Ω, which describe the location of the resonance and its spectral width. These values given as angular frequencies can be transformed to the wavelength using the following relations:

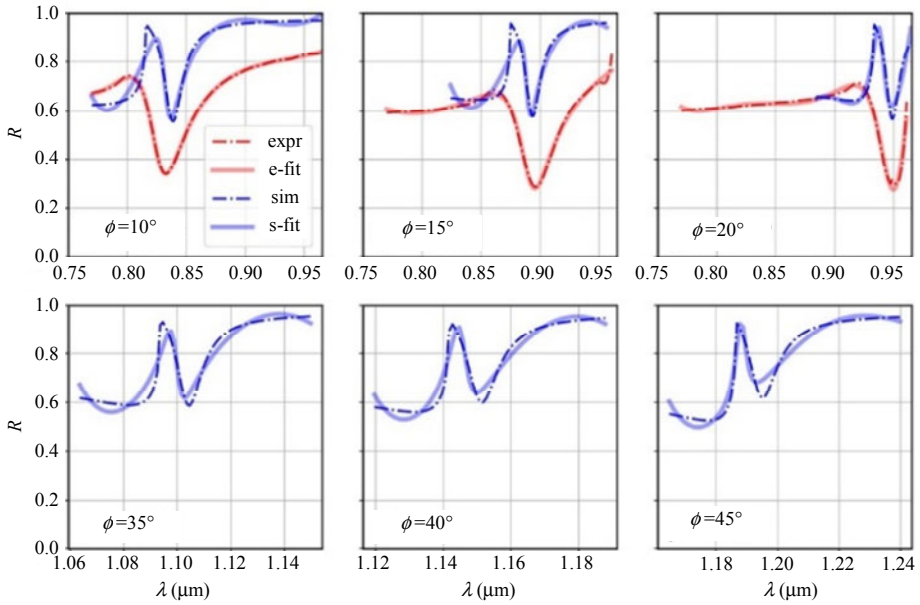

Fig. 5 Spectral reflectance for the device under analysis in the near infrared range. In the first row, the experimental results (expr) are plotted in red dashed-dotted line with its fitting (e-fit) as a solid semitransparent red line. The simulated response (sim) is given as a blue dashed-dot line with the fitting (s-fit) as a solid semitransparent blue line. The first row contains three plots for angles of incidence ϕ=10º, 15º, and 20º. In this first row, we have maintained the same spectral range. The second row only contains the simulated results that go beyond the spectral range of our spectrometer. We can see that the resonance is red-shifted when increasing the angle of incidence. The horizontal axis for these simulations' changes for each angle of incidence.

$$\lambda_0 = \frac{2\pi c}{\omega_0}, \tag{3}$$

$$\delta\lambda = 2\pi c \frac{\Omega}{\omega_0}, \tag{4}$$

where $\delta\lambda$ describes the spectral width of the resonance.

Figure 6 represents the evolution of these two parameters for the visible (in blue) and the near infrared (in red). The dots correspond with the experimental values and the solid lines are for the simulation. We check that the computational electromagnetic model fits very well with the location for λ_0, and generates a spectral width that is narrower than that in the experimental, as shown in Figs. 4 and 5. These two parameters are important when defining the sensitivity and the FOM of refractometric sensors in Section 4.

4. Refractometric sensor performance

The results reported in the previous section support the use of this structure as a refractometric sensor based on SPRs. To prove this application, we have evaluated the sensing performance of the system using the variation of spectral reflectivity with the index of refraction of the analyte medium. The plasmonic structure and the analyte are placed

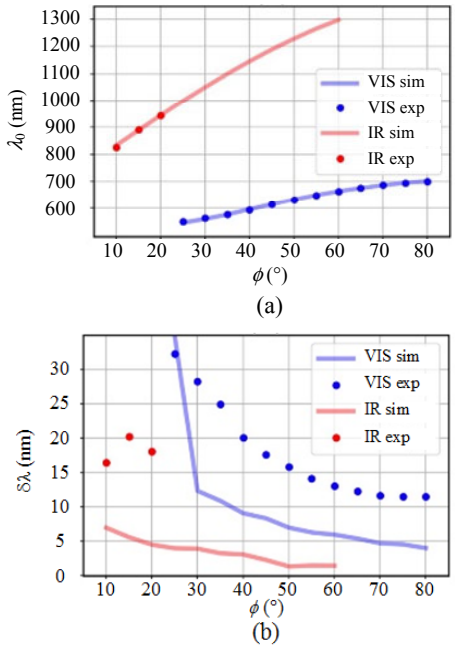

Fig. 6 Variation of the central wavelength λ_0 and spectral width for the resonances in (a) Fig. 4 and (b) Fig. 5 as a function of the angle of incidence, ϕ. The results for the visible are represented in blue and the values for the infrared are in red. The dots denote the experimental values and the solid lines are for the results obtained from simulation.

inside a glass cell filled with the liquid analyte. The angle of incidence on the cell is corrected to account for the effect of Snell's law on the angle of incidence when light refracts through the measurement cell. Both the measurements and simulations have been performed for an angle of incidence ϕ=47º.

Figure 7(a) shows the experimental and simulated spectral reflectivities for three analytes.

The parameters to characterize the performance of a refractometric sensor are the sensitivity (s) and FOM, which are defined as:

$$s = \frac{\delta\lambda_{\min}}{\delta n_a}, \tag{5}$$

$$\mathrm{FOM} = \frac{s}{\delta\lambda}, \tag{6}$$

where $\lambda_{\min}$ is the wavelength at the minimum value of the reflectivity and n_a is the index of refraction of the analyte [54].

Using the results from Fig. 7(a), we obtain these characteristics parameters as $s_{\mathrm{exp}} \approx s_{\mathrm{sim}}$=600 nm/RIU, $\mathrm{FOM}_{\mathrm{exp}}$=30 RIU^{-1}, and $\mathrm{FOM}_{\mathrm{sim}}$=75 RIU^{-1}. These values already reach the theoretical maximum sensitivity, S. For the Kretschmann configuration, it is 600 nm/RIU [55]. As we do in the previous section, the reliability of our numerical model makes it possible to expand the analysis of the device beyond the limitations of our experimental setup. Then, maintaining the same illumination conditions, we have also simulated the spectral response in the infrared when varying the index of refraction of the analyte within a given range, $n_a \in [1.330, 1.375]$. The results are plotted in Fig. 7(b).

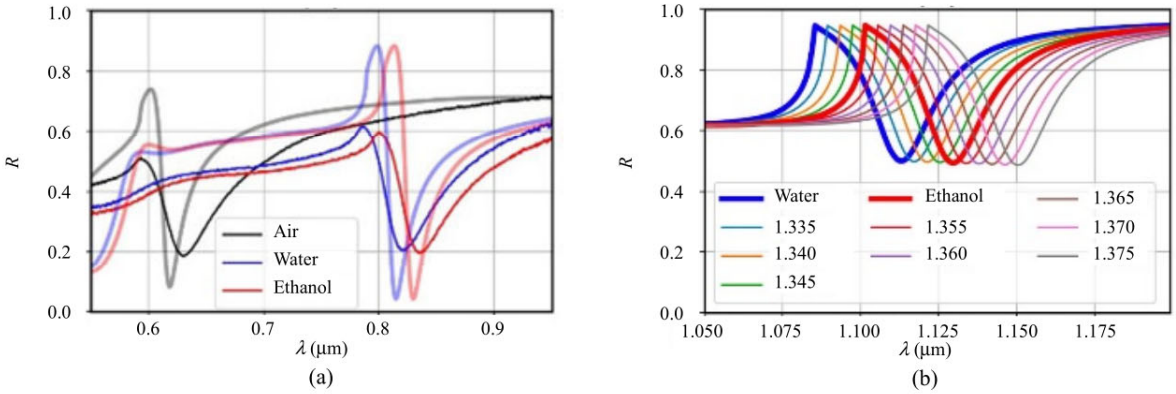

Fig. 7 Spectral reflectance: (a) experimental (dark colors) and simulated (light colors) spectral reflectance of the structure for three analytes (air, water, and ethanol) and (b) simulated spectral reflectance in the near infrared for a liquid analyte with the index of refraction $n_a \in [1.330, 1.375]$.

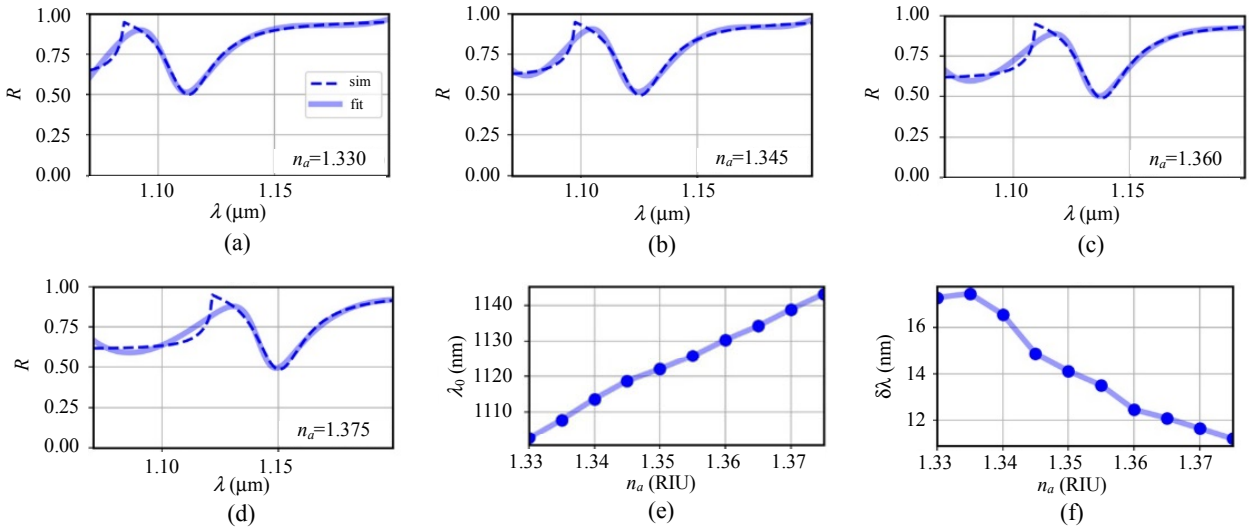

Fig. 8 Infrared spectral reflectance: (a)–(d) simulated spectral reflectance (sim) in the near infrared (dashed line) and fitting (fit) to the Fano model (solid transparent line) of (2) for n_a=1.330, n_a=1.345, n_a=1.360, and n_a=1.375, respectively, and (e) and (f) dependence of the central wavelength, λ_0, and width of the resonance, δλ, as a function of the index of refraction of the analyte.

Then, knowing that the spectral width of the SPR decreases with the wavelength, these reflectances have been fitted with the model in (2) to obtain the central wavelength of the resonance, λ_0, and its width, δλ. The fitting of the simulated spectra to the model is presented in Figs. 8(a)–8(d) for four values of $n_a \in (1.330, 1.345, 1.360, 1.375)$, respectively. The values of λ_0 and δλ obtained from the fitting are also represented in Figs. 8(e) and 8(f) as a function of the index of refraction of the analyte. Using these values, we can calculate the sensing parameters as s=880 nm/RIU and FOM=80 RIU^{-1}. Both parameters are larger than those in the visible region and exceed the limit of the Kretschmann configuration.

5. Conclusions

Laser ablation has become a reliable and competitive fabrication tool for nano-structured devices. By controlling the laser pulse parameters, ablation modifies the metal surface in a predictive manner to shape it in the form of the LIPSS. In fact, our fabrication setup produces a split LIPSS with a shallow dip on the top of the periodic grating. We have modeled the fabricated topography with the addition of two super Gaussian functions: one for the wide variation of the LIPSS and the other one for replicating the middle dip of the structure. The parameters of this geometry are adjusted to replicate the actual fabricated profile.

From a physical point of view, when the LIPSS nanostructure is illuminated, the SPRs excited in these LIPSSs are coherently combined with the diffractive response of the periodic pattern. We have shown that these resonances are well described and accurately fitted within the spectral range around the resonance, as a Fano response. The parameters obtained from the fitting, especially the value of the central wavelength and its spectral width, produce lineshapes that are redshifted and narrow when increasing the angle of incidence, both in the visible and the near infrared, and also both for the experimental results and simulations.

The refractometric performance of our device has been experimentally tested. We have measured the spectral response for a fixed angle of incidence ϕ=47º and for three analytes: air, water, and ethanol. The measurement results have been compared with the results obtained from the simulation. Again, the agreement between simulated and experimental results is very good when considering the central wavelength of the resonance, with the simulation predicting a narrower peak than that observed

experimentally. This discrepancy is likely caused by the departure between the ideal geometry and the actual topography, and by the irregularities in the period and shape over the illuminated region of the device. Even in the current conditions, the performance of the device surpasses the values of the Krestchmann configuration. When extending our simulations into the near infrared, the sensing capabilities increase, and the expected performance is again very promising.

In summary, refractometry of liquids can take advantage of the nano-structured surface fabricated with a low-cost and high-throughput technology, and the femtosecond laser ablation, which generates the LIPSS in a quite reliable way. These nanostructures generate the SPRs that become the Fano resonances, allowing a better determination of the optical constant of analytes.

Declarations

Conflict of Interest The authors declare that they have no competing interests.

References

[1] I. Staude and J. Schilling, "Metamaterial-inspired silicon nanophotonics," *Nature Photonics*, 2017, 11(5): 274–284.

[2] K. Fan, R. D. Averitt, and W. J. Padilla, "Active and tunable nanophotonic metamaterials," *Nanophotonics*, 2022, 11(17): 3769–3803.

[3] A. Li, S. Singh, and D. Sievenpiper, "Metasurfaces and their applications," *Nanophotonics*, 2018, 7(6): 989–1011.

[4] W. A. Murray and W. L. Barnes, "Plasmonic materials," *Advanced Materials*, 2007, 19(22): 3771–3782.

[5] X. Fan, W. Zheng, and D. J. Singh, "Light scattering and surface plasmons on small spherical particles," *Light: Science & Applications*, 2014, 3(6): e179-e179.

[6] C. Battaglia, C. M. Hsu, K. Soderstrom, J. Escarré, F. J. Haug, M. Charriere, *et al*., "Light trapping in solar cells: can periodic beat random?" *ACS Nano*, 2012, 6(3): 2790–2797.

[7] T. Lee, J. Kim, I. Koirala, Y. Yang, T. Badloe, J. Jang, *et al*., "Nearly perfect transmissive subtractive coloration through the spectral amplification of Mie scattering and lattice resonance," *ACS Applied Materials & Interfaces*, 2021, 13(22): 26299–26307.

[8] S. Z. Sekhi, M. Shokooh-Saremi, and M. M. Mirsalehi, "Ultra-broadband, wide-angle, and polarization-insensitive metamaterial perfect absorber for solar energy harvesting," *Journal of Nanophotonics*, 2020, 14(4): 046014–046014.

[9] L. T. Xu, M. Chen, Y. H. Weng, K. X. Xie, J. Wang, S. H. Cao, *et al*., "Label-free fluorescent nanofilm sensor based on surface plasmon coupled emission: in situ monitoring the growth of metal-organic frameworks," *Analytical Chemistry*, 2022, 94(17): 6430–6435.

[10] U. Mogera, H. Guo, M. Namkoong, M. S. Rahman, T. Nguyen, and L. Tian, "Wearable plasmonic paper-based microfluidics for continuous sweat analysis science advances," *American Association for the Advancement of Science*, 2022, 8(12): eabn1736.

[11] D. Barshilia, A. C. Komaram, P. C. Chen, L. K. Chau, and G. E. Chang, "Slab waveguide-based particle plasmon resonance optofluidic biosensor for rapid and label-free detection analyst," *Royal Society of Chemistry*, 2022, 147(20): 4417–4425.

[12] A. Gade, A. Sharma, N. Srivastava, and S. Flora, "Surface plasmon resonance: a promising approach for label-free early cancer diagnosis," *Clinica Chimica Acta*, 2022, 527: 79–88.

[13] M. Mohseni-Dargah, Z. Falahati, B. Dabirmanesh, P. Nasrollahi, and K. Khajeh, "*Machine learning in surface plasmon resonance for environmental monitoring*," in Artificial Intelligence and Data Science in Environmental Sensing, M. Asadnia, A. Razmjou, and A. Beheshti, Eds., London: Academic Press, 2022: 269–298.

[14] M. S. Brown and C. B. Arnold, "*Fundamentals of laser-material interaction and application to multiscale surface modification*," in Laser Precision Microfabrication, K. Sugioka, M. Meunier, and A. Piqué, Eds., Berlin: Springer, 2010: 91–120.

[15] T. Kurita, K. Komatsuzaki, and M. Hattori, "Advanced material processing with nano-and femto-second pulsed laser," *International Journal of*

Machine Tools and Manufacture, 2008, 48(2): 220–227.

[16] J. Choi and C. Schwarz, "Advances in femtosecond laser processing of optical material for device applications," *International Journal of Applied Glass Science*, 2020, 11(3): 480–490.

[17] A. Klos, X. Sedao, T. E. Itina, C. Helfenstein-Didier, C. Donnet, S. Peyroche, *et al*., "Ultrafast laser processing of nanostructured patterns for the control of cell adhesion and migration on titanium alloy," *Nanomaterials*, 2020, 10(5): 864

[18] C. Kunz, S. Engel, F. A. Müller, and S. Gräf, "Large-area fabrication of laser-induced periodic surface structures on fused silica using thin gold layers," *Nanomaterials*, 2020, 10(6): 1187.

[19] D. Zhang, R. Liu, and Z. Li, "Irregular LIPSS produced on metals by single linearly polarized femtosecond laser," *International Journal of Extreme Manufacturing*, 2021, 4(1): 015102.

[20] I. Gnilitskyi, T. J. Y. Derrien, Y. Levy, N. M. Bulgakova, T. Mocek, and L. Orazi, "High-speed manufacturing of highly regular femtosecond laser-induced periodic surface structures: physical origin of regularity," *Scientific Reports*, 2017, 7(1): 8485.

[21] S. Sheta, M. S. Afgan, L. Jiacen, W. Gu, Z. Hou, and Z. Wang, "Insights into enhanced repeatability of femtosecond laser-induced plasmas," *ACS Omega*, 2020, 5(47): 30425–30435.

[22] Y. Zhang, Q. Jiang, K. Cao, T. Chen, K. Cheng, S. Zhang, *et al*., "Extremely regular periodic surface structures in a large area efficiently induced on silicon by temporally shaped femtosecond laser," *Photonics Research*, 2021, 9(5): 839–847.

[23] A. San-Blas, M. Martinez-Calderon, E. Granados, M. Gómez-Aranzadi, A. Rodríguez, and S. M. Olaizola, "LIPSS manufacturing with regularity control through laser wavefront curvature," *Surfaces and Interfaces*, 2021, 25: 101205.

[24] J. Sládek, K. Hlinomaz, I. Mirza, Y. Levy, T. J. Derrien, M. Cimrman, *et al*., "Highly regular LIPSS on thin molybdenum films: optimization and generic criteria," *Materials*, 2023, 16(7): 2883.

[25] J. Bonse and S. Gräf, "Ten open questions about laser-induced periodic surface structures," *Nanomaterials*, 2021, 11(12): 3326.

[26] X. Liu, D. Du, and G. Mourou, "Laser ablation and micromachining with ultrashort laser pulses," *IEEE Journal of Quantum Electronics*, 1997, 33(10): 1706–1716.

[27] D. Breitling, A. Ruf, and F. Dausinger, "Fundamental aspects in machining of metals with short and ultrashort laser pulses," *Proceeding of SPIE*, *Photon Processing in Microelectronics and Photonics III*, 2004, 5339: 49–63.

[28] F. Dausinger, H. Hugel, and V. I. Konov, "Micromachining with ultrashort laser pulses: from basic understanding to technical applications," in *ALT'02 International Conference on Advanced Laser Technologies*, Adelboden, 2003, pp. 106–115.

[29] Y. Zhang, X. Wang, K. Yan, H. Zhu, B. Wang, and B. Zou, "Laser micro/nano-structuring pushes forward smart sensing: opportunities and challenges," *Advanced Functional Materials*, 2022, 33(8): 2211272.

[30] E. Skoulas, A. C. Tasolamprou, G. Kenanakis, and E. Stratakis, "Laser induced periodic surface structures as polarizing optical elements," *Applied Surface Science*, 2021, 541: 148470.

[31] J. Bonse, S. V. Kirner, and J. Krüger, "*Laser-induced periodic surface structures (LIPSS)*," in Handbook of Laser Micro-and Nano-Engineering, K. Sugioka, Eds., Cham: Springer, 2020: 1–59.

[32] D. Dufft, A. Rosenfeld, S. Das, R. Grunwald, and J. Bonse, "Femtosecond laser-induced periodic surface structures revisited: a comparative study on ZnO," *Journal of Applied Physics*, 2009, 105(3): 034908.

[33] M. Handrea-Dragan and I. Botiz, "Multifunctional structured platforms: from patterning of polymer-based films to their subsequent filling with various nanomaterials," *Polymers*, 2021, 13(3): 445.

[34] S. Durbach, F. T. Krauss, M. Hoffmann, V. Lehmann, H. Reinhardt, J. Sundermeyer, *et al*., "Laser-driven one-and two-dimensional subwavelength periodic patterning of thin films made of a metal-organic MoS_2 precursor," *ACS Nano*, 2022, 16(7): 10412–10421.

[35] M. Vlahou, F. Fraggelakis, P. Manganas, G. D. Tsibidis, A. Ranella, and E. Stratakis, "Fabrication of biomimetic 2D nanostructures through irradiation of stainless steel surfaces with double femtosecond pulses," *Nanomaterials*, 2022, 12(4): 623.

[36] H. Sun, J. Li, M. Liu, D. Yang, and F. Li, "A review of effects of femtosecond laser parameters on metal surface properties," *Coatings,* 2022, 12(10): 1596.

[37] I. Gnilitskyi, W. Alnusirat, M. Sorgato, L. Orazi, and G. Lucchetta, "Effects of anisotropic and isotropic LIPSS on polymer filling flow and wettability of micro injection molded parts," *Optics & Laser Technology*, 2023, 158: 108795.

[38] M. H. Elshorbagy, L. M. Sánchez-Brea, J. Buencuerpo, J. del Hoyo, Á. Soria-García, V. Pastor-Villarrubia, *et al*., "Polarization conversion using customized subwavelength laser-induced periodic surface structures on stainless steel," *Photonics Research*, 2022, 10(9): 2024–2031.

[39] A. Sharma, D. Marla, S. S. Joshi, and R. Bathe, "A study of femtosecond laser processed microtextures on silicon wafers to enhance optical absorption," *Lasers in Manufacturing and Materials Processing*, 2022, 9(3): 277–291.

[40] H. Wang, F. Zhang, and K. Yin, "Bioinspired antireflective subwavelength nanostructures induced by femtosecond laser for high transparency glass,"

Journal of Non-Crystalline Solids, 2023, 600: 122016.

[41] S. Mamykin, I. Gnilitskyi, M. Dusheyko, T. DeVol, and V. Bliznyuk, "Femtosecond laser nano-structuring for surface plasmon resonance-based detection of uranium," *Applied Surface Science*, 2022, 576: 151831.

[42] R. A. Hughes, E. Menumerov, and S. Neretina, "When lithography meets self-assembly: a review of recent advances in the directed assembly of complex metal nanostructures on planar and textured surfaces," *Nanotechnology*, 2017, 28(28): 282002.

[43] A. A. S. Falah, W. R. Wong, and F. R. M. Adikan, "Single-mode eccentric-core D-shaped photonic crystal fiber surface plasmon resonance sensor," *Optics & Laser Technology*, 2022, 145: 107474.

[44] M. H. Elshorbagy, A. Cuadrado, G. González, F. J. González, and J. Alda, "Performance improvement of refractometric sensors through hybrid plasmonic-fano resonances," *Journal of Lightwave Technology*, 2019, 37(13): 2905–2913.

[45] M. H. Elshorbagy, A. Cuadrado, B. Garcia-Camara, R. Vergaz, J. A. Gómez-Pedrero, and J. Alda, "Ultra-narrow spectral response of a hybrid plasmonic-grating sensor," *IEEE Sensors Journal*, 2019, 20(7): 3520–3528.

[46] J. Bonse and S. Gräf, "Maxwell meets Marangoni – a review of theories on laser-induced periodic surface structures," *Laser & Photonics Reviews*, 2020, 14(10): 2000215.

[47] S. Hou, Y. Huo, P. Xiong, Y. Zhang, S. Zhang, T. Jia, *et al.*, "Formation of long- and short-periodic nanoripples on stainless steel irradiated by femtosecond laser pulses," *Journal of Physics D: Applied Physics*, 2011, 44(50): 505401.

[48] A. Bijalwan and V. Rastogi, "Design and simulation of a palladium-aluminum nanostructure-based hydrogen sensor with improved figure of merit," *IEEE Sensors Journal*, 2019, 19(15): 6112–6118

[49] I. Saleem and W. K. Chu, "Gold nano-ripple structure with potential for bio molecular sensing applications," *Sensing and Bio-Sensing Researc*h, 2016, 11: 14–19.

[50] P. B. Johnson and R. W. Christy, "Optical constants of the noble metals," *Physical Review B*, 1972, 6(12): 4370.

[51] S. Roh, T. Chung, and B. Lee, "Overview of the characteristics of micro-and nano-structured surface plasmon resonance sensors," *Sensors*, 2011, 11(12): 1565–1588.

[52] J. Homola, I. Koudela, and S. S. Yee, "Surface plasmon resonance sensors based on diffraction gratings and prism couplers: sensitivity comparison," *Sensors and Actuators B: Chemical*, 1999, 54 (1–2): 16–24.

[53] M. Vala, K. Chadt, M. Piliarik, and J. Homola, "High-performance compact SPR sensor for multi-analyte sensing," *Sensors and Actuators B: Chemical*, 2010, 148(2): 544–549.

[54] K. M. Mayer and J. H. Hafner, "Localized surface plasmon resonance sensors," *Chemical Reviews*, 2011, 111(6): 3828–3857.

[55] D. W. Huang, Y. F. Ma, M. J. Sung, and C. P. Huang, "Approach the angular sensitivity limit in surface plasmon resonance sensors with low index prism and large resonant angle," *Optical Engineering*, 2010, 49(5): 054403.